Particle Ordering in Colloidal Thin Films Deposited by Flow-Coating

Cindy Y. Lau and William B. Russel
Dept. of Chemical and Biological Engineering, Princeton University, Princeton, NJ 08544

DOI 10.1002/aic.14413
Published online March 4, 2014 in Wiley Online Library (wileyonlinelibrary.com)

The wide applications of two-dimensionally ordered nanoscale features have stimulated the development of cheap and fast fabrication techniques in recent years. We achieved large area of uniform film of nanoparticles between 49.8 ± 8.7 and 117.6 ± 6.7 nm via flow-coating. However, the single crystalline domains of a close-packed monolayer remained limited. That motivated deposition of initially ordered colloidal dispersions, attained through deionized solutions to extend electrostatic double layers for long-range repulsion. Although the deposition agreed reasonably well with our power-law model, the initial order was destroyed at high shear. While the particle order was partially preserved during deposition at low shear, the domain size was not particularly extensive due to the high compression of double layers during evaporation. © 2014 American Institute of Chemical Engineers *AIChE J*, 60: 1287–1302, 2014
Keywords: flow-coating, colloids, self-assembly, monolayer, colloidal crystal

Introduction

Two-dimensional (2-D) ordered structures with submicron features have diverse applications, including photonic band-gap materials for waveguides,[1,2] structural coloring,[3] antireflective surfaces,[3] biomimetic materials with water repellent surfaces,[4,5] sensors,[6,7] storage media,[8–10] light emitting diodes,[11,12] templates for lithography,[13,14] and electrophoresis devices that sort macromolecules according to size and mobility.[15,16] This motivates the development of cheap and fast methods to fabricate large arrays. These techniques are generally divided into top-down and bottom-up approaches, where the former creates small features from a larger one and the latter creates patterns from smaller building blocks.

Top-down techniques are usually lithographic, for example, photolithography,[17–19] e-beam lithography,[20,21] and nanoimprint lithography,[22,23] which have a high level of precision and reproducibility. However, these processes involve expensive equipment that increase both fabrication time and cost. On the other hand, bottom-up approaches such as colloidal assembly[24] create nanostructures with a variety of properties by using building blocks with different functionalities. Continuing advancement in particle synthesis provides cheap monodisperse nanoparticles as small as 3.2 nm.[25–31] Assembly methods for creating 2-D structures include electrophoretic deposition,[32,33] spin-coating,[34,35] dip-coating,[36,37] and adsorption,[38,39] each with its advantages and disadvantages. For example, electrophoretic deposition is flexible in the shape of the substrate but limited with aqueous solutions when high voltage is needed. Spin-coating and dip-coating are both fast but waste material during the process, while adsorption produces a monolayer easily but is very chemistry-specific. Therefore, we are drawn to flow-coating (sometimes called doctor blade coating), a modified dip-coating process that is inexpensive, fast, simple, and robust across a variety of solutions and substrates.[40–54] The horizontal configuration of flow-coating eliminates gravitational drainage, an undesirable feature of dip-coating (Figure 1). Furthermore, holding the sample between the substrate and blade reduces the amount of materials required significantly.

Two characteristic deposition strategies in flow-coating depend simply on the experimental velocity. At low velocity, evaporation dominates and the deposition is typically referred to as convective assembly. On the other hand, evaporation is delayed at high velocity and the deposition is governed by a combination of viscous drag and capillary pressure. This high velocity regime, where the effect of evaporation on the thickness of deposition is negligible, is typically referred to as Landau–Levich deposition.[55] We see the potential of Landau–Levich deposition[56–61] as a faster and more easily controlled process than convective assembly[46–54] in achieving a colloidal monolayer. Therefore, our goal was to achieve an extensive monolayer of ordered nanoparticles by Landau–Levich deposition with a flow-coating setup.

In this article, we flow-coated silica and polystyrene colloids with diameters between 50 and 120 nm. Although silica of comparable size has been dip-coated by Brewer et al.,[56] the order of the deposited particles was not investigated. Furthermore, they were unable to predict the deposition due to the complexity of gravitational drainage in their vertical setup. On the contrary, our deposition confirms with a model for the deposition and permits a study of the order.

We were further motivated to use initially ordered dispersions to improve the 2-D order of the final structure.

Correspondence concerning this article should be addressed to W. B. Russel at wbrussel@princeton.edu.

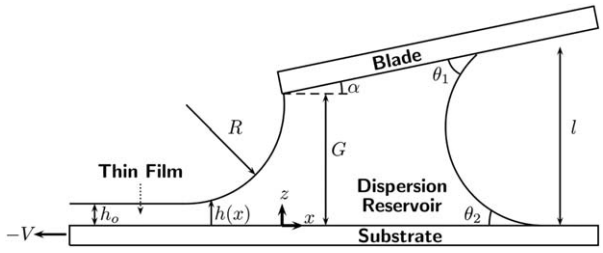

Figure 1. Schematics of flow-coating experiments.

Deionizing the dispersions produces double layers with thickness $\kappa^{-1}=\sqrt{\epsilon_o \epsilon k_B T/\Sigma_{j=1}^{N} n_j q_j^2}$, where ϵ_o is the vacuum permittivity, ϵ is the dielectric constant of the solution, k_B is the Boltzmann constant, T is the solution temperature, n_j and q_j are the number density and charge of free ionic species j, respectively.[62] Electrostatic repulsion rearranges the colloids spontaneously into an ordered structure to minimize the free energy.[63–65] If the colloidal crystal has submicron separations, bright iridescence will appear as a result of Bragg diffraction.[65–67] That iridescence is a convenient indicator of the presence of colloidal crystals.[68,69]

Model for Landau–Levich Deposition

In the Landau–Levich regime, the balance between viscous drag and capillary pressure determines the ultimate thickness of the deposited film. We modified their model for dip-coating in our horizontal configuration,[55] in which gravitational drainage is negligible. At steady state, the Stokes equation describes the flow

$$0=-\nabla p+\nabla\cdot\boldsymbol{\tau} \tag{1}$$

with p the pressure and $\boldsymbol{\tau}$ the stress tensor. Because the horizontal characteristic length scale is much larger than the vertical in the thin film region, the lubrication approximation can be applied, reducing Eq. 1 to

$$0=-\frac{dp}{dx}+\frac{d\tau_{xx}}{dx}+\frac{d\tau_{xz}}{dz} \tag{2}$$

where x and z are the horizontal and vertical directions, respectively (Figure 1).

The pressure $p=-\gamma/R$, determined by the dispersion surface tension γ and radius of curvature R (Figure 1), which can be approximated by $1/R\approx(d^2h/dx^2)/(1+(dh/dx)^2)^{1.5}\approx d^2h/dx^2$ according to the lubrication approximation. The deionized dispersion flows like a power-law fluid with a shear-dependent viscosity $\eta=k\dot{\gamma}^{n-1}$, where $\dot{\gamma}$ is the shear rate, k the flow consistency index, and n the power law index, while the Newtonian behavior of the nondeionized dispersion can be retrieved with $n=1$. The shear stress follows as $\tau=k\dot{\gamma}^n=k(du/dz)^n$, with u the velocity in the x direction.

Substituting the above expressions into Eq. 2 and applying the lubrication approximation suggests that the second term on the right becomes negligible, resulting in Eq. 3a. Using the no-slip boundary condition at the substrate ($u|_{z=0}=-V$) and a stress-free boundary condition at the surface ($(du/dz)|_{z=h}=0$), we obtain du/dz (Eq. 3b) and u (Eq. 3c)

$$0=\gamma\frac{d^3h}{dx^3}+\frac{d}{dz}\left(k\left(\frac{du}{dz}\right)^n\right)\Rightarrow\frac{d}{dz}\left(\frac{du}{dz}\right)^n=-\frac{\gamma}{k}\frac{d^3h}{dx^3} \tag{3a}$$

$$\frac{du}{dz}=\left(\frac{\gamma}{k}\frac{d^3h}{dx^3}(h-z)\right)^{1/n} \tag{3b}$$

$$u=-V+\left(\frac{\gamma}{k}\frac{d^3h}{dx^3}\right)^{1/n}\left(\frac{1}{1/n+1}\right)\left(h^{1/n+1}-(h-z)^{1/n+1}\right) \tag{3c}$$

We are particularly interested in the uniform thin film thickness $h(x\to-\infty)=h_o$ before significant evaporation occurs, at which the volumetric flow rate per unit width can be approximated as $Q=-Vh_o$. This flow rate should be conserved outside of the uniform film, giving

$$\int_o^h u dz=-Vh_o \quad\Rightarrow\quad h'''h^{1+2n}=\frac{k}{\gamma}V^n(1/n+2)^n(h-h_o)^n \tag{4}$$

Equation 4 can be made dimensionless as Eq. 5 with the scaling factors in Eq. 6, with primes indicating the derivatives with respective to x. In fact Eq. 5 is applicable to the nondeionized dispersion when substituting $n=1$ for a Newtonian fluid and replacing k with the shear-independent viscosity μ

$$\bar{h}'''\bar{h}^{1+2n}=(\bar{h}-1)^n \tag{5}$$

$$\bar{x}=\frac{x}{\left(\frac{h_o^{2+n}\gamma}{kV^n(1/n+2)^n}\right)^{1/3}}\ \text{and}\ \bar{h}=\frac{h}{h_o} \tag{6}$$

For the case of $n=1$, a linear perturbation of the nearly uniform film, $\bar{h}_{\bar{x}\to-\infty}=1+\delta\bar{h}$, simplifies Eq. 5 to $\delta\bar{h}'''\approx\delta\bar{h}$. Because the film is decaying in the negative $\bar{x}$ direction, the analytical solution suggests that $\delta\bar{h}\approx\delta\bar{h}'\approx\delta\bar{h}''\approx ce^{\bar{x}}$ for some constant c. The resultant boundary conditions for Eq. 5 in the thin film ($\bar{x}\to-\infty$) becomes $\bar{h}\approx1+ce^{\bar{x}}, \bar{h}'\approx ce^{\bar{x}}$, and $\bar{h}''\approx ce^{\bar{x}}$. As guided by this reasoning, we impose the boundary conditions at a sufficiently negative $\bar{x}$ (Eq. 7), namely, $-\bar{x}_{\text{large}}$, and numerically integrate with the shooting method using Mathematica (Wolfram)

$$\bar{h}|_{\bar{x}=-\bar{x}_{\text{large}}}=1+ce^{-\bar{x}_{\text{large}}} \tag{7a}$$

$$\bar{h}'|_{\bar{x}=-\bar{x}_{\text{large}}}=ce^{-\bar{x}_{\text{large}}} \tag{7b}$$

$$\bar{h}''|_{\bar{x}=-\bar{x}_{\text{large}}}=ce^{-\bar{x}_{\text{large}}} \tag{7c}$$

with c a constant so that $ce^{-\bar{x}_{\text{large}}}$ is small.

Previous studies show that the thin film thickness h_o can be predicted correctly by matching this asymptotic value with the radius of curvature of the static meniscus.[55,70–73] In particular, the result from the lubrication approximation holds as long as the capillary number $Ca\equiv\eta V/\gamma$ is smaller than $O(10^{-3})$. For our system, the matching occurs at the blade edge ($x=x_o$) where the film thickness equals to the gap height G and the radius of curvature R can be measured. In dimensionless terms

$$\bar{h}''|_{\bar{x}=\bar{x}_o}=h_o^{(1+2n)/3}\left(\frac{\gamma}{kV^n(1/n+2)^n}\right)^{2/3}\frac{1}{R} \tag{8a}$$

$$\bar{h}|_{\bar{x}=\bar{x}_o}=\frac{G}{h_o} \tag{8b}$$

We found that $\bar{h}''$ at our relevant $\bar{x}_o$, obtained by imposing the two conditions in Eq. 8 simultaneously, satisfies an asymptotic value $\bar{h}''|_{\bar{x}=\bar{x}_o}=-1.1n^3+3.1n^2-3.7n+2.4$ (Figure 2b). Therefore, the thickness of the uniform film is given by

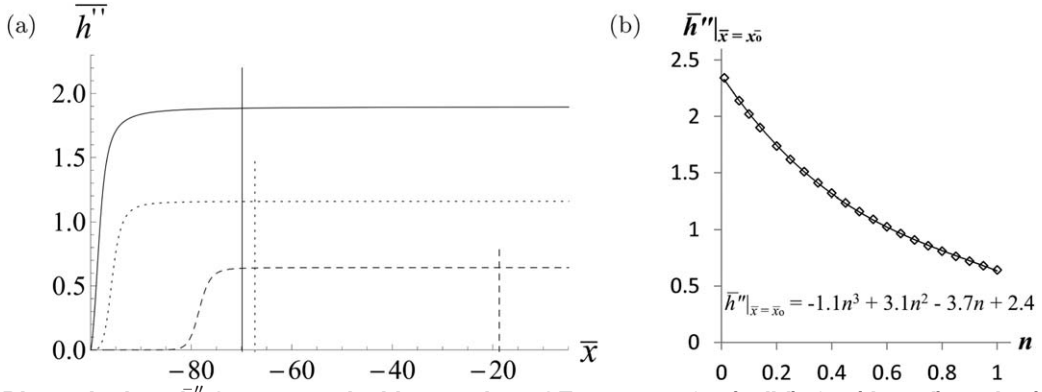

Figure 2. (a) Dimensionless $\bar{h}''$ from numerical integration of Eq. 5 at n=0.1 (solid), 0.5 (dotted), and 1 (dashed).

Vertical lines indicate their respective $\bar{x}_o$. (b) Relationship between $\bar{h}''|_{\bar{x}=\bar{x}_o}$ and n.

$$h_o=\left[\left(-1.1n^3+3.1n^2-3.7n+2.4\right)R\right]^{3/(1+2n)}\left(\frac{kV^n(1/n+2)^n}{\gamma}\right)^{2/(1+2n)} \tag{9}$$

which reduces to Eq. 10 for a Newtonian fluid with $k=\mu$ and $n=1$

$$h_o=0.64R\left(\frac{3\mu V}{\gamma}\right)^{2/3} \Longleftrightarrow \frac{h_o}{R}=1.33Ca^{2/3} \tag{10}$$

It is usually easier to measure the meniscus in the reservoir in the right of Figure 1. Its radius of curvature is $l/(\cos\theta_1+\cos\theta_2)$,[41,74] with l the height and θ_1 and θ_2 the two contact angles. As the lateral pressure gradient within the reservoir is negligible in our system, we obtain R by equating the radii of curvature in the left and right menisci as $R=l/(\cos\theta_1+\cos\theta_2)$.

A particularly important parameter for the deionized colloids is the shear rate $\dot{\gamma}=du/dz$, which affects the viscosity as mentioned previously. According to Eq. 3b, the shear rate at any x is largest at $z=0$, which gives

$$\dot{\gamma}|_{z=0}=\left(\frac{\gamma}{k}h'''h\right)^{1/n}=\frac{(1/n+2)V}{h_o}(\bar{h}'''\bar{h})^{1/n} \tag{11}$$

As shown in Figure 3, maximum of $(\bar{h}\bar{h}''')^{1/n}$ is 0.250 regardless of n. Hence, the maximum shear rate is

$$\dot{\gamma}_{\max}=\frac{0.250(1/n+2)V}{h_o} \tag{12}$$

Experimental Details

Characterization of colloidal dispersion

Silica particles (SiO_2, MP1040, 55 wt %, Nissan Chemical) and polystyrene particles (PS, AGB-5108, 50 wt %, Rohm and Haas) in water were used as received for experiments with nondeionized dispersions. Their diameters (d), measured by scanning electron microscopy (SEM), are 117.6 $\pm$ 6.7 nm and 109.7 $\pm$ 7.6 nm, respectively. We also tested the robustness of flow-coating with polydisperse aqueous 50-nm silica particles (49.8 $\pm$ 8.7 nm, Snowtex-OL, Nissan Chemical). To simplify notations, SiO_2 and PS colloids mentioned in this article refer to 118-nm SiO_2 and 110-nm PS, respectively, unless specified otherwise.

In some experiments, these SiO_2 and PS colloids were deionized to produce colloidal crystals. The dispersions were first diluted with Milli-Q water (18.2 MΩ-cm, Millipore Corp.) to about 30 v/v % and then mixed with 5 w/v % ion exchange resin (AG 501-X8, Bio-Rad) on a stirrer for 2 h. The resin was then removed through centrifugation (4000 rpm, 5 min) and the supernatant was diluted to the desired volume fraction with Milli-Q water.

The surface tension of the dispersion (γ) was measured with a Wilhelmy plate (TR516, Nima Technology) and the electrophoretic mobility of particles was determined with a zetasizer (Zetasizer Nano ZS, Malvern). The viscosities of the nondeionized dispersions at various volume fractions were measured by a capillary viscometer (H505, Cannon Instrument), whereas the shear-dependent rheological properties of the colloidal crystals were characterized by a rheometer (MCR 501, Anton Paar) with a concentric cylinder geometry (CC27-C-PTD200). The latter measurements imposed either the shear rates ($\dot{\gamma}$) between 1 and 4000/s or shear stress (τ) between 0.1 and 40 Pa. Shear sweeps in both increasing and decreasing directions were recorded to observe any hysteresis. Any test that did not reach steady state as indicated by the software (RheoPlus), usually at low τ, was ignored.

Preparation of colloidal dispersions and substrate for flow-coating

The colloidal dispersions were diluted to the desired volume fractions (ϕ), typically between 0.047 and 0.134, with Milli-Q water for the flow-coating experiments. Silicon wafers and glass slides, which were used as substrates and blades in the flow-coating experiments, were immersed in piranha solution (concentrated sulfuric acid and hydrogen

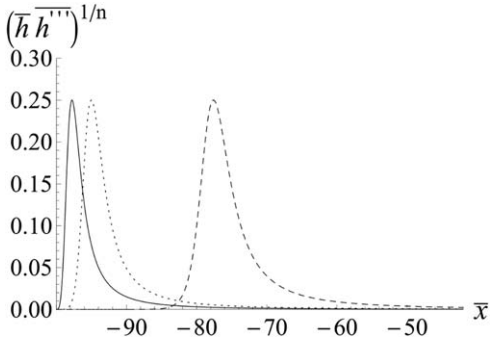

Figure 3. Dimensionless $(\bar{h}\bar{h}''')^{1/n}$ from numerical integration of Eq. 5 at n = 0.1 (solid), 0.5 (dotted), and 1 (dashed).

Maximum of $(\bar{h}\bar{h}''')^{1/n}$ is 0.250 regardless of n.

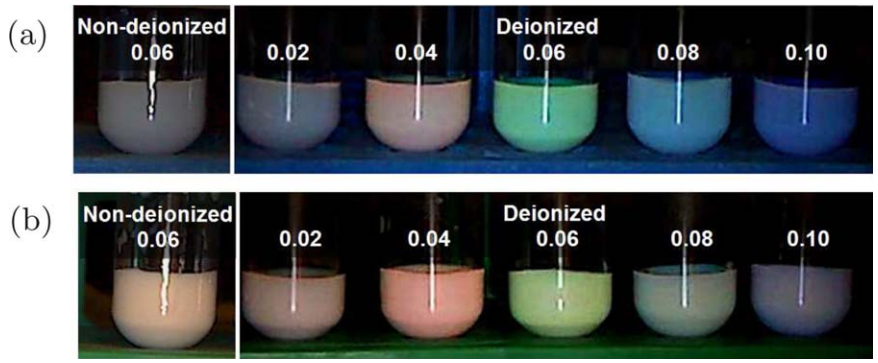

Figure 4. Nondeionized and deionized (a) SiO_2 and (b) PS at various ϕ.

(left to right) Nondeionized dispersion at ϕ=0.06, deionized dispersions at ϕ=0.02, 0.04, 0.06, 0.08, and 0.10. [Color figure can be viewed in the online issue, which is available at wileyonlinelibrary.com.]

peroxide in a volume ratio of 7 to 3) at about 70°C for 20 min, followed by DI water rinsing and air blow-drying. (Caution: piranha solution is very energetic and potentially explosive. Proper personal protective equipment must be worn at all times and the peroxide should be added to the acid in an open container in the hood.)

Flow-coating deposition and analysis

In a flow-coating experiment, a silicon substrate was taped to the motor stage, whose speed was controlled by a motion controller (ESP300, Newport). A glass slide was held at an angle (α), typically around 6°, to serve as the blade. After adjusting the gap (G) to the desired height with a micrometer, the colloidal dispersion was pipetted between the blade and the substrate, which acts as the reservoir. The typical gap of 200–550 μm held solution volumes between 22 and 52 μL. The stage moved at speeds between 0.02 and 3.8 mm/s, depositing a film with stripes of different thicknesses on the substrate that dried within a few seconds. Pictures of the setup and videos of the deposition processes taken through a USB microscope (26700-300, Aven) provided measures of parameters such as G, l, θ_1, and θ_2 (Figure 1) with the software ImageJ (NIH).

The SEM (Quanta 200 ESEM, FEI) images of the dried samples were analyzed with ImageJ to obtain the fractional projected areal coverage (a). Furthermore, the maximum single crystalline domain size of the particles in a 6.5 μm by 6.5 μm SEM image was determined with a Matlab (MathWorks) program (Supporting Information). In brief, we first determined the orientation of the crystalline domain using a code modified from Johnston-Peck et al.[35] and Hillebrand et al.[75] and then applied a code to measure the domain size, as defined by particles with six nearest neighbors that are oriented within $\pm 3^{\circ}$ of a common angle.

We also estimated the evaporation rate (E, kg/s) by measuring the mass loss rate of water in a container with known dimensions. In some experiments, the evaporation rate E was suppressed through covering the deposited film or pumping humidified gas into a nearly closed chamber containing the deposited film.[76] As the duration of each flow-coating experiment is too short to measure the evaporation rate *in situ*, the reduction in E was measured in a separate experiment.

Experimental Results

Colloidal crystal formation through deionization

Our colloids formed colloidal crystals upon deionization with the ion-exchange resin. As shown in Figure 4, the deionized dispersions exhibited red iridescence at ϕ=0.04, green iridescence at ϕ=0.06, and blue iridescence at ϕ=0.08 and 0.10, indicating the presence of colloidal crystals. Red, green, and blue correspond to wavelengths of about 670, 530, and 470 nm, respectively,[77] suggesting separations between particles decreasing from ϕ=0.04 to ϕ=0.10 as the soft double layer repulsion allows closer approach at higher volume fractions. To demonstrate that the iridescence is a good indicator of order, we include the translucent white nondeionized SiO_2 and milky white nondeionized PS dispersions in Figure 4 for contrast. We used colloidal dispersions with distinct red and green iridescence in our flow-coating experiments.

Particle characterization

Surface Tension. The surface tension of nondeionized SiO_2 dispersions was 71.1 ± 0.8 mN/m, independent of concentration between the most dilute ($\phi = 0.021$) and the most concentrated stock ($\phi = 0.343$). This is the surface tension of water within experimental error (71.5 ± 0.9 mN/m). However, the average surface tension of nondeionized PS dispersions was smaller than water at 62.4 ± 0.8 mN/m for the stock (ϕ=0.485), indicating the presence of surfactants. Upon dilution with Milli-Q water for flow-coating experiments ($0.039 \leq \phi \leq 0.071$), the effect of surfactant was reduced, producing a slightly higher surface tension of 66.1 ± 0.5 mN/m.

On the other hand, while deionizing has insignificant effect on the surface tension of SiO_2 dispersions between ϕ=0.033 and 0.075, leading to an average value (71.9 ± 0.6 mN/m) the same as water within experimental error, its effect on the PS dispersions is more prominent. However, deionization does remove most of the surfactant in the PS stock (62.4 mN/m), increasing the surface tension of the deionized PS between ϕ=0.039 and 0.065 to an average of 70.8 ± 0.7 mN/m, the same as water within experimental error.

Rheological Measurements. The viscosities (μ) of the nondeionized SiO_2 and PS dispersions measured with a capillary viscometer at 21°C at shear rates around 225/s were normalized on the viscosity of water (μ_o) (Figure 5). The standard deviations of less than 1.5% for all measurements were too small to be displayed. The volume fraction dependence of the relative viscosity (μ/μ_o) fitted by $\mu_r = 1.0 + 3.1\phi + 8.4\phi^2$ is shown by the solid line. The positive deviation from the 2.5ϕ- and the $5.9\phi^2$-virial terms for hard spheres are evidence of significant primary and secondary

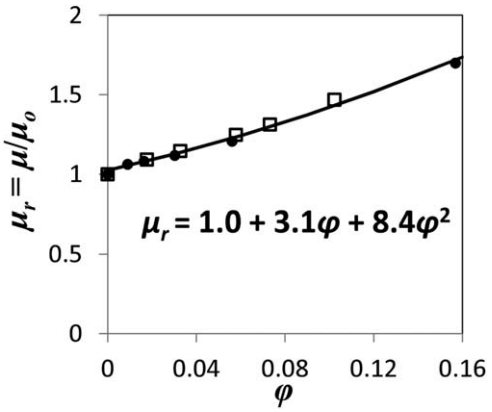

Figure 5. Relative viscosities of SiO_2 (□) and PS (●) dispersions.

The solid line indicates the second-order polynomial fit to the data.

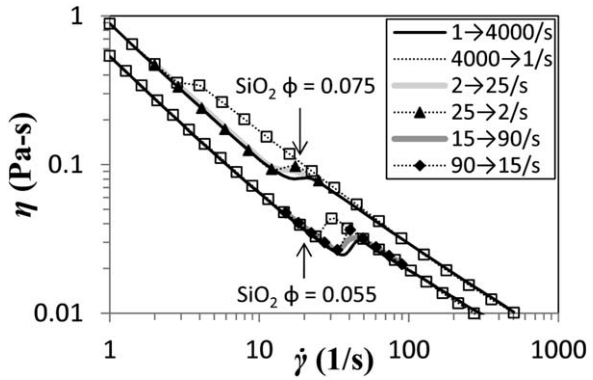

Figure 7. Viscosities of deionized SiO_2 dispersions (ϕ=0.055 and 0.075) cycling between low and high shear rates.

Solid lines indicate increasing sweeps and symbols indicate decreasing sweeps.

electroviscous effects, respectively.[78,79] The Peclet number $Pe=3\pi\mu_o(d/2)^3\dot{\gamma}/k_BT \sim 0.6$, with $\dot{\gamma}$ the shear rate, d the particle diameter, k_B the Boltzmann constant, and T the temperature, suggests that the measurements is close to the low shear limit.[80,81]

The viscosities of deionized dispersions were measured at shear rates between 1 and ~400/s with a rheometer with a concentric cylinder geometry to avoid the turbulent flow transition according to Taylor's prediction[82] ($\dot{\gamma}_{crit}$). The deionized dispersions differed considerably from the non-deionized counterparts, that is, shear-thinning until (and most likely beyond) the onset of turbulence flow (Figure 6). We characterized the deionized dispersions as power-law fluids described by $\eta=k\dot{\gamma}^{n-1}$. Figure 6 illustrates that the steepness of the slope decreases discontinuously as the shear rate increases, which corresponds to an increase in n, resulted from the progressive destruction of crystalline structure by the increasing viscous stress.

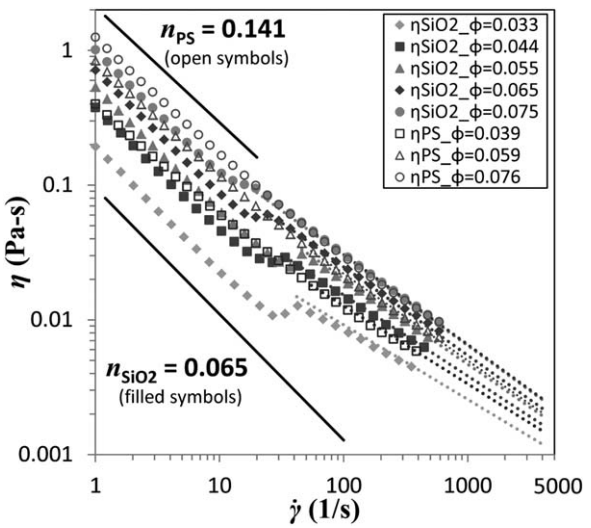

Figure 6. Viscosities of deionized SiO_2 (filled symbols) and PS (open symbols) colloidal dispersions.

High shear rate data are truncated at their respective $\dot{\gamma}_{crit}$. Dotted lines are derived experimental fits in the high shear rate regime. The average slope between 1 and 5/s is −0.935 for SiO_2 and −0.859 for PS, converting into n of 0.065 and 0.141.

In the low shear regime between 1 and 5/s (Figure 6), n is relatively constant. The average slope in the $\log\eta - \log\dot{\gamma}$ plot is -0.935 ± 0.008 for SiO_2 and -0.859 ± 0.021 for PS, converting into n_{low} of 0.065 and 0.141, respectively. The small n, especially for SiO_2, suggests a colloidal crystal with relatively elastic behavior. The ordered structure of the colloidal crystal is most likely intact at such low shear.[83]

Beyond the low shear regime, the dispersion continues to shear-thin but n increases discontinuously, suggesting that the colloidal crystal breaks down and deviates from the elastic behavior. Although the viscosity of the PS dispersions decreases monotonically, there is a sudden increase for the SiO_2 around 20/s (Figure 6). This is most likely associated with an abrupt change to a less ordered structure, commonly known as shear melting.[84,85] The viscosity, a measure of resistance to flow, is relatively low for a colloidal crystal because of its ordered structure. On shear melting, the disordered structure hinders the deformation more; hence the order-disorder transition produces a jump in viscosity. This jump is reversible, i.e., independent of shear direction. The viscosity retraces itself when cycling between low and high shear rates except around jumps (Figure 7). This hysteresis supports the jump as an order-disorder transition that appears at similar locations in both directions but with a larger variation while ramping down (symbols). In fact, the order-disorder transition (ramping up) takes 51 ± 7 s, whereas the disorder-order transition (ramping down) takes systematically longer time with a larger variation at 112 ± 34 s. Clearly, the destruction of order by shear is faster than formation of order from disorder.

At rates above the jump, shear-thinning resumes and the viscosities of SiO_2 and PS converge. In fact, if we establish the ϕ-dependence of n and k for PS dispersions from 55 to 386/s, namely, n_{high} and k_{high}, respectively, and apply them to the SiO_2 dispersions, the calculated values (dotted lines in Figure 6) match the experimental data very well. As the viscosities of SiO_2 and PS are almost identical in this high shear regime, one might deduce that SiO_2 and PS behave similarly in their disordered states. This contrasts with the low shear regime where the lower viscosity and n of SiO_2 suggest a more ordered structure than PS (Figure 6). We extrapolate the viscosity in this regime ($\eta=k_{high}\dot{\gamma}^{n_{high}-1}$) to shear rates beyond $\dot{\gamma}_{crit}$ as the real viscosity cannot be determined due to turbulence.

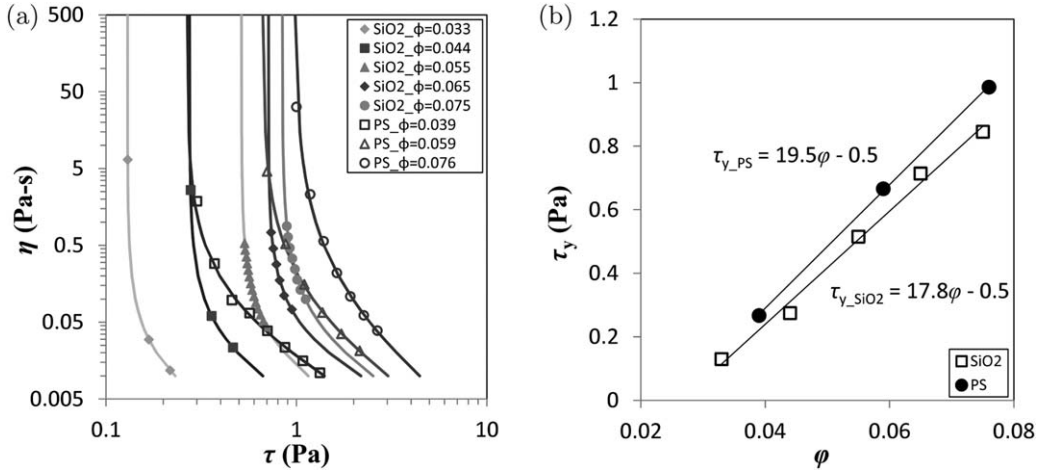

Figure 8. (a) The viscosity and shear stress of SiO_2 (filled symbols) and PS (open symbols) dispersions.

The fitted lines (solid lines) are used to determine the dynamic yield stresses τ_y. (b) The estimated τ_y are plotted as a function of ϕ.

The dynamic yield stresses τ_y of deionized colloids can be obtained from the rheological measurements. Below the yield stress, the colloidal crystal behaves like an elastic solid and has minimal flow (if any).[86] Once τ_y is exceeded, the flow becomes considerable and a smaller viscosity results. Plotting the viscosity against the shear stress (Figure 8a) demonstrates that each sample approaches a separate vertical tangent at low shear. We estimated τ_y with these asymptotic values by a power-law fit (solid lines) and obtained comparable values with literature.[87] The linear increase with ϕ (Figure 8b) shows that PS has a slightly larger τ_y than SiO_2 of the same ϕ.

Thickness of film deposited by flow-coating of nondeionized dispersions

Comparison Between Theoretical and Experimental Film Thickness. Nondeionized SiO_2 and PS dispersions at various volume fractions were successfully deposited using a flow-coating system. A typical dried film is shown in Figure 9a, where the thickness within each step of constant velocity, shown as a vertical stripe, is quite uniform. In particular, films with uniform thickness covering area up to 10 cm^2 have been achieved. We note that this has not exhausted the instrumental limit and may have the potential to cover even larger area. The difference in shade of the stripes reflects the difference in thickness.

To determine quantitatively the thickness (h_{expt}), we first obtain the fractional areal coverage of deposited particles (a) in the SEM images (Figure 9b). As the particles are never found to stack on each other below monolayer coverage, we can relate the two quantities as follows. The total projected area of particles in a wet film with area A_{wet} is aA_{wet}; hence, the number of particles is $N=aA_{wet}/(d^2\pi/4)$ and the total volume they occupy is $N(d^3\pi/6)$. We can relate this volume to the wet film volume ($A_{wet}h_{expt}$) through the volume fraction of particles (ϕ). Therefore, we obtained the relationship $h_{expt}=2ad/(3\phi)$, where $a=0.906$ for a hexagonally close-packed monolayer. We multiplied a obtained at low magnifications (Figure 9b) by 0.906, which assumes hexagonal close-packing in the brighter area containing deposited particles, before applying it to the equation to correct for the inability to resolve individual particles and interstitial sites.

Figure 10a shows the thickness h_{expt}, normalized on the radius of curvature of the static meniscus R, for SiO_2 films deposited at various capillary numbers $Ca \equiv \mu V/\gamma$. Here, h_{expt} was systematically thicker than h_{th} (Eq. 10) by a factor of 2.07 ± 0.18 for dispersions with $\phi \geq 0.071$ (open symbols) and slightly less for dispersions with smaller ϕ (filled symbols). Le Berre et al. also observed roughly two times thicker films in their experiments with phospholipid solutions and attributed the effect to the Marangoni effect.[41] As the surface concentration of surfactant decreases from the reservoir to the film due to stretching of the interface,[88,89] the gradient provokes a Marangoni stress that results in thickening.[90,91] The extent of thickening, known to be within a factor of 2.52,[90–92] with the maximum being reached when the surface moves at the substrate velocity. This might not seem immediately relevant to our system as surfactant should be minimal in the SiO_2 dispersions which have a surface tension similar to water. However, it is the surfactant gradient at the surface that is important. To assess the effect, we follow the dimensional analysis of Ramdane and Quéré[90] to evaluate the surface tension difference ($\Delta\gamma$) required to provide a significant thickening flux. When surfactant is present at the film surface, the stress generated by the surface tension gradient must be balanced by shear stresses

$$\mu \frac{du}{dz}|_{z=h} = \frac{d\gamma}{dx}|_{z=h} \tag{13}$$

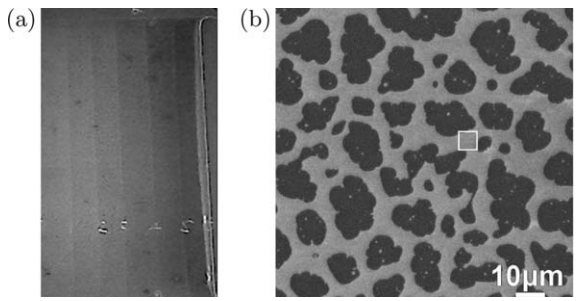

Figure 9. (a) A typical film deposited at steps of increasing velocity (left to right).

(b) SEM image of a typical submonolayer of particles. Brighter regions correspond to deposited particles, whereas darker regions correspond to bare silicon substrate. The white box represents the typical size and location of where subsequent SEM images are taken.

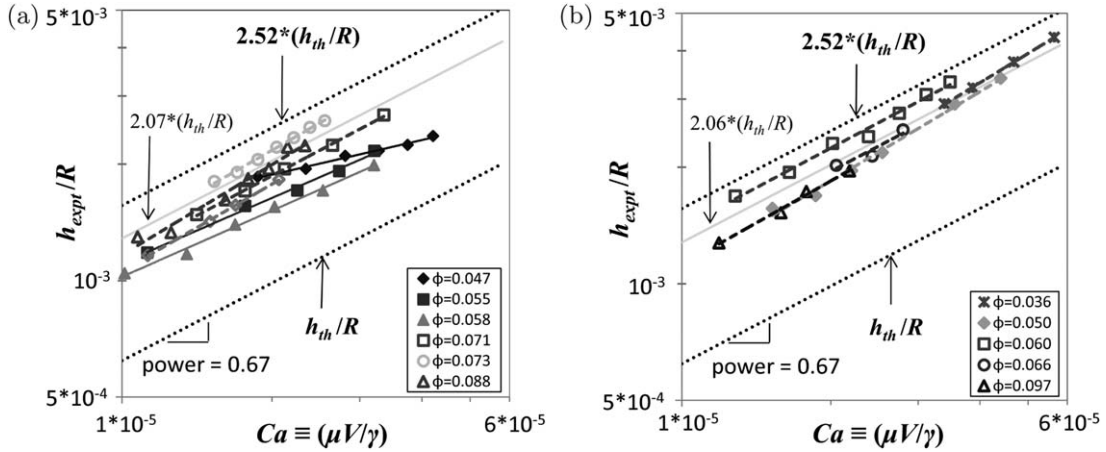

Figure 10. The dimensionless experimental film thickness h_{expt}/R of nondeionized (a) SiO_2 and (c) PS at various capillary number $Ca \equiv \mu V/\gamma$.

The bottom dotted line indicates normalized theoretical thickness h_{th} from Eq. 10 and the top dotted line indicates theoretical upper bound of thickening (thickening factor = 2.52).

A scaling analysis with length scales in Eq. 6 leads to

$$\frac{\mu V}{h_o} \sim \frac{\Delta\gamma}{h_o(\gamma/(3\mu V))^{1/3}} \tag{14}$$

$$\Delta\gamma \sim 3^{-1/3}\gamma\left(\frac{\mu V}{\gamma}\right)^{2/3} \tag{15}$$

With typical experimental values $\mu \sim O(10^{-3}\text{Pa-s})$, $\gamma \sim O(10^{-1}\text{N/m})$, and $V \sim O(10^{-3}\text{m/s})$, the surface tension difference necessary for a significant thickening flux is as small as $O(10^{-5}\text{N/m})$. Although not resolvable in our measurements of the surface tension, there could be sufficient residual surfactant from synthesis to generate the effect. Therefore, thickening from surfactant-driven Marangoni stress could affect deposition of nominally surfactant-free SiO_2 dispersions.

Furthermore, Park[92] also shed light on the effect of surfactant on the power dependence between h/R and Ca. The thickening factor was found to depend on the Marangoni number $M = -(\Gamma_o/\gamma_o)(\partial\gamma/\partial\Gamma)_{\Gamma_o}$, where Γ is the surfactant surface concentration and the subscript o indicates the values at the reservoir. The theoretical dimensionless film thickness, scaled by $\sqrt{2}R$, at various M and Ca is shown in Figure 11. The degree of thickening varies with M. For example, for Ca between 10^{-5} and 10^{-3}, the thickening factor remains at its upper limit (2.52) for a sample with larger M (i.e., $M=0.1$). As a result of uniform thickening, the power dependence of the film thickness on velocity remains the same as $h/R \sim Ca^{0.67}$ in Eq. 10. However, the thickening factor for a sample with smaller M (i.e., $M=0.01$) decreases gradually as Ca increases.

In fact, our dispersions at different concentrations have various M. If Γ_o changes more significantly than γ_o and $(\partial\gamma/\partial\Gamma)_{\Gamma_o}$ upon dilution, the more concentrated dispersion will have a larger M and vice versa. We approximate the M for our more diluted dispersions with the literature value of $O(10^{-2})$ for stearic acid with low surface concentration (1/100 the number of molecules required to form a close-packed film).[93] Together with the observation in the previous paragraph, we expect the deposition from dispersions with higher $\phi(M \sim 0.1)$ to result in $h/R \sim Ca^{0.67}$, whereas that from smaller $\phi(M \sim 0.01)$ to have a smaller exponent for deposition between $Ca=10^{-5}$ and 10^{-3}. Our films, typically deposited around $Ca \sim O(10^{-5})$, indeed show a comparable dependence of $h/R \sim Ca^{0.74\pm0.04}$ for SiO_2 dispersions with $\phi \geq 0.071$ and lower powers for dispersions with smaller ϕ (Figure 10a).

Results show that nondeionized PS dispersions deposit similarly as SiO_2, producing films thicker than prediction by 2.06 ± 0.45 times and with a power dependence of 0.74 ± 0.05 on Ca (Figure 10b). The only major difference is that the thickening factor is constant for PS within the range $0.036 \leq \phi \leq 0.097$, presumably due to the larger concentration of surfactant in the PS dispersions that results in a larger surface concentration and M. Figure 11 shows that a larger M provides a wider range of Ca at which the thickening remains constant, which the thickening of our PS resembles.

To test the applicability of the flow-coating technique with smaller particles, we used 50-nm silica particles. Like the

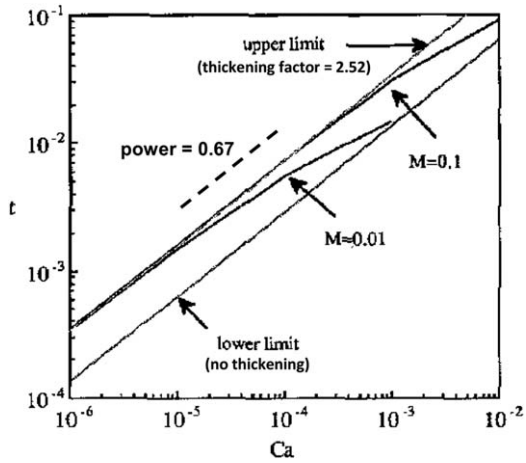

Figure 11. The dimensionless theoretical film thickness $t \equiv h_{th}/(\sqrt{2}R)$ as a function of Ca at various M.

The lower limit indicates no thickening and upper limit indicates maximum thickening (thickening factor = 2.52). Figure reprinted from *J Colloid Interface Sci*, 146, Park CW, Effects of insoluble surfactants on dip coating, 382–394, Copyright 1991, with permission from Elsevier.

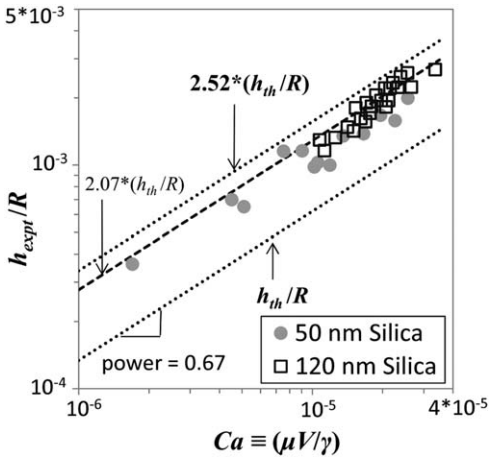

Figure 12. The dimensionless film thickness h_{expt}/R of nondeionized 50 and 118 nm SiO_2, with thickening explained by the Marangoni effect.

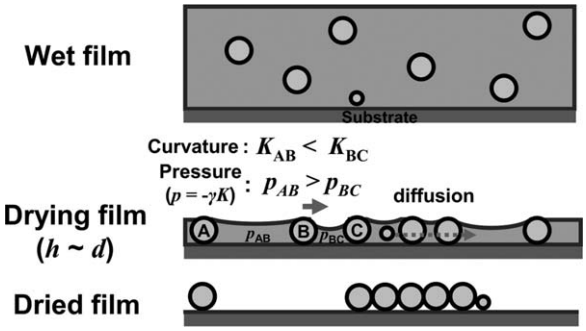

Figure 14. Schematics of ordering of nondeionized particles during drying of deposited film.

118-nm SiO_2, the deposited thickness follows the theory (Eq. 10) with a thickening factor of ~2.07 times, explained by the Marangoni effect (Figure 12). Therefore, deposition by flow-coating can be extended to smaller particles.

Particles ordering in flow-coated nondeionized samples

To quantify the ordering of deposited particles, we identify particles with six nearest neighbors oriented within $\pm 3^{\circ}$ from each other using the Matlab code (Supporting Information) to determine the largest domain in a 6.5 μm by 6.5 μm image. The maximum domain size varies roughly inversely proportional to the areal coverage a (Figure 13). When the wet film is thicker than the diameter of the particles d, the particles are free to move three-dimensionally. During evaporation, the film thickness decreases uniformly as suggested by the homogeneous a across the film, except near the edges where the pinned contact lines foster evaporation and result in coffee stain effect.[94] When the thickness becomes comparable to d, the particle motion is confined in a 2-D plane. The correlation of maximum domain size with a but not h (not shown) suggests that ordering most likely takes place when the film is thinned to $\lesssim O(d)$, where a remains constant. The large uncovered (dark) area at submonolayer coverage (Figure 9b) also implies that there is minimal interaction between the particles and substrate that potentially hinders particle motion over a large distance.

Figure 14 depicts particle ordering during film drying. When the film thickness is slightly thinner than d, the film is no longer uniform and the partially protruded particles create curved menisci that provide capillary pressures. This pressure is more negative where the packing is denser.[95] For example, particle B in Figure 14 is closer to particle C than particle A, resulting in a meniscus with larger curvature (K) between particles B and C and a lower capillary pressure ($p = -\gamma K$). The lateral pressure gradient across particle B attracts it toward particle C, nucleating a domain. If the overall coverage is low, particles approaching an existing domain have more time to rearrange into their lowest energy, i.e., ordered, position before being immobilized by other incoming particles. Therefore, the maximum domain size is larger for smaller a and vice versa (Figure 13). The observation that the capillary pressure gradient facilitates the formation of 2-D crystal is in agreement with previous studies.[96,97]

Some smaller particles are evident in the SEM images (Figure 13, right). Instead of intermixing with the majority of larger particles, they segregate to the edge of large domains. As the film becomes about the thickness of d, the meniscus will first form between larger particles and pull them together. Although the larger particles are confined two dimensionally, the wet film is thick enough for the free movement of smaller particles.[98] Additionally, the higher diffusivity of the smaller particles facilitates diffusion away from ordered domains of larger particles to minimize overall energy. Hence, the smaller particles tend to form grain

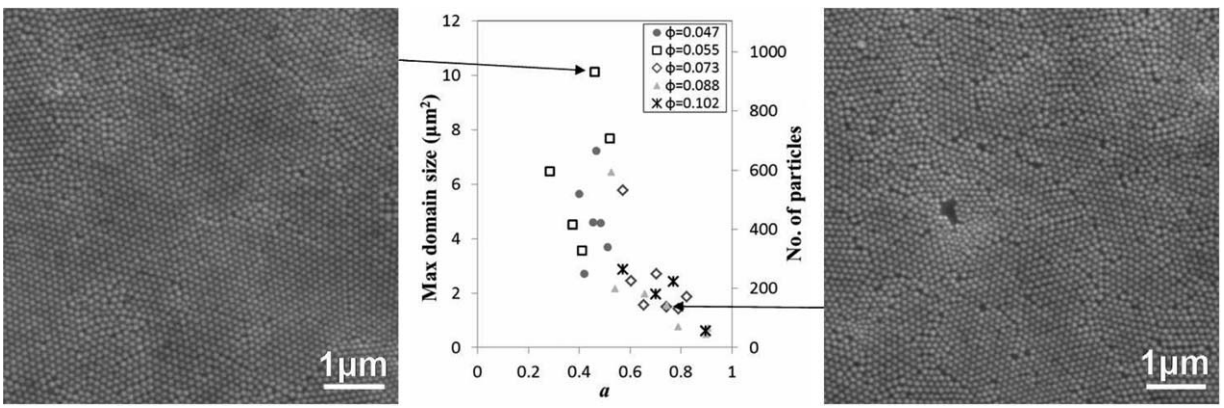

Figure 13. The maximum domain size in a 6.5 μm by 6.5 μm SEM image of nondeionized SiO_2.

The maximum domain size is inversely correlated with the projected areal coverage a (middle). SEM images of deposited SiO_2 with low (left) and high (right) overall coverages.

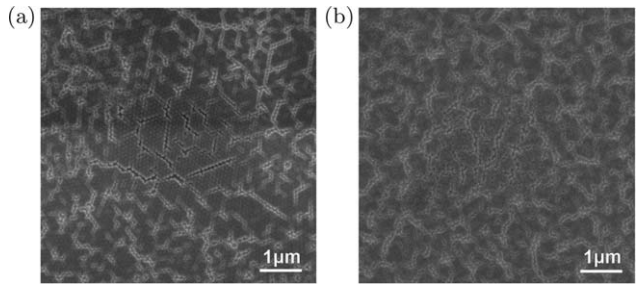

Figure 15. SEM images of deposited nondeionized PS with (a) low and (b) high overall coverage.

boundaries or their own domains instead of integrating with the larger particles.

PS particles form fairly small domains ($\sim 0.5\ \mu m^2$) even at low coverage (Figure 15a). This is most likely due to the hydrophobicity of PS that leads to a larger contact angle than the hydrophilic SiO_2. As a result, the meniscus formed as the particles protrude has a smaller curvature,[99] which reduces the pressure difference between particles. The diminished attraction restricts particle coalescence and nucleation of large domains.

Last, the SEM images of SiO_2 and PS monolayers are shown in Figure 16. Although the particle ordering of SiO_2 (Figure 16a) is slightly better than PS (Figure 16b), the domain sizes are very limited in both monolayers ($\sim 0.61 \pm 0.11 \mu m^2$ for SiO_2 and $\sim 0.37 \mu m^2$ for PS). This shows that a large monolayer of ordered particles cannot be achieved by the Landau–Levich deposition of nondeionized colloids with this flow-coating setup. Therefore, we were motivated to extend the flow-coating technique to depositing colloidal crystals, achieved through deionizing the colloidal dispersions, as an effort to translate the existing particle order into the resultant film.

Strategies in depositing deionized ordered colloids

Landau–Levich Deposition at Low Shear. As deionized colloids lose order at high shear rates (Figure 6), we need to deposit at low shear rates to preserve the original crystalline order. Equations 9 and 12 show that $\dot{\gamma}_{max}$ depends on R, V, γ, n, and k, yet only R and V are easily tunable experimentally. Figure 17 plots $\dot{\gamma}_{max}$ within the range of typical experimental inputs at some fixed n_{high} and k_{high} from the previous section. Clearly, a lower shear in the Landau–Levich regime can be achieved by decreasing the velocity V and/or increasing radius of meniscus R, where the latter can be achieved by increasing the gap height G, blade angle α, and dispersion volume.

On the other hand, a lower evaporation rate E is supposed to shift the transition between evaporative and Landau–Levich regimes to lower velocities. Therefore, we suppressed evaporation by two different methods, through covering the sample or pumping humidified air into the chamber. These methods reduced evaporation by 32 and 73%, respectively. The resultant conditions indeed allowed Landau–Levich deposition at low shear using large R and even lower V.

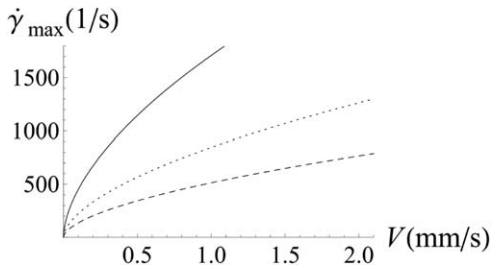

Figure 17. The maximum shear rate $\dot{\gamma}_{max}$ given by Eqs. 12 and 9 at $R=250\mu m$ (solid), 375 μm (dotted), and 500 μm (dashed) with $\phi=0.055, \gamma=72 mN/m, n=n_{high}$ and $k=k_{high}$.

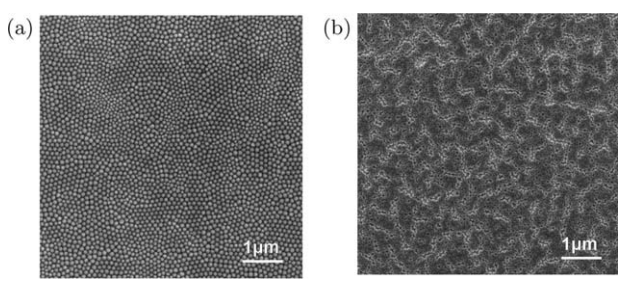

Figure 16. SEM images of nondeionized (a) SiO_2 and (b) PS at monolayer coverages.

Effect of Initial Sample Loading. Other than being a function of deposition shear rate as expected, we found that flow-coating of deionized colloids also depends greatly on the initial sample loading in the reservoir. For dispersions that are loaded at a single point, strong iridescence is usually found around the point of loading and weak iridescence is found further away (Figure 18a). The strong iridescence implies an ordered structure near the source, whereas the weaker iridescence suggests that the colloids become less ordered as they are forced to flow away from the source. However, if the loading is delocalized along the blade edge, which minimizes the distance that the dispersion has to travel, strong iridescence is rather uniform (Figure 18c). We will delocalize the loading for depositing large areas of colloidal crystal, but will also use the samples with nonuniform iridescence to compare the effect.

We demonstrate that the difference in ordering, i.e., iridescence, also affects the deposited film thickness using samples with initially localized iridescence like the one shown in Figure 18a. Deposition at various volume fractions confirms that the region with highly ordered colloids (filled symbols in Figure 18b) produces thinner films with a larger exponent on V when compared to moderately ordered colloids (open symbols in Figure 18b) deposited identically. Uniform highly ordered colloids also show a consistent $h-V$ relationship (Figure 18d).

Deposition of deionized moderately ordered colloids

Comparison Between Theoretical and Experimental Film Thicknesses. We first consider films from moderately ordered colloids. As the deposition is usually associated with weakly iridescent to noniridescent dispersions, we expect the power law index n to be close to unity. However, we only established n and k as functions of ϕ for $55/s \lesssim \dot{\gamma} \lesssim 386/s$ due to Taylor instability in Couette measurements (Figure 6). We assume that n and k remain unchanged above 386/s. However, we also expect the colloidal dispersions to behave like Newtonian fluids above some high shear rate $\dot{\gamma}_o$, like the nondeionized dispersions with relative viscosity $\mu_r = 1.0 + 3.1\phi + 8.4\phi^2$ (Figure 5) and $n = 1$. Such a transition, where $k_{high}\dot{\gamma}_o^{n_{high}-1}$ approaches μ, typically occurs at $\dot{\gamma}_o \sim O(10^4/s)$ for the relevant ϕ. However, the determination of shear rates

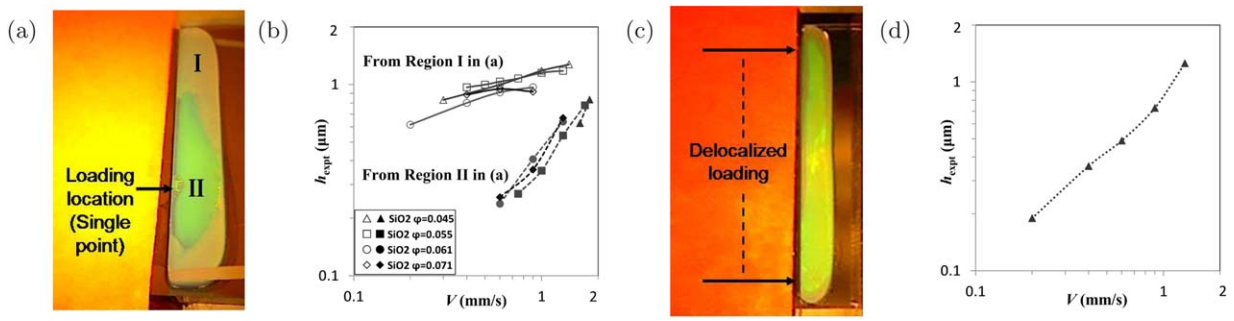

Figure 18. Top view of deionized SiO_2 dispersion sandwiched between the transparent blade and substrate showing (a) nonuniform iridescence from localized loading and (c) uniform iridescence from delocalized loading.

The representative thicknesses of their deposited films are shown in (b) and (d), respectively. The open and filled symbols in (b) correspond to deposition from moderately ordered [region I in (a)] and highly ordered [region II in (a)] colloids, respectively. [Color figure can be viewed in the online issue, which is available at wileyonlinelibrary.com.]

in our flow-coating experiments requires prior knowledge of n, which we lack, as $\dot{\gamma}=(1/n+2)0.250V/h_o$ (Eq. 12). Therefore, we estimated it by comparing an experimental parameter $0.250V/h_{\text{expt}}$ from flow-coating with a scaled shear rate $\dot{\gamma}/(1/n+2)$ according to Eq. 12. In particular, our assumption suggests that $n=n_{\text{high}}$ for $\frac{55/\text{s}}{(1/n_{\text{high}}+2)} < \frac{0.250V}{h_{\text{expt}}} < \frac{\dot{\gamma}_o}{(1/n_{\text{high}}+2)}$ and the shear rate in flow-coating follows as $\frac{(1/n_{\text{high}}+2)0.250V}{h_{\text{expt}}}$. We indeed found that our experiments were all performed within this range.

Figure 19a shows that the experimental film thicknesses agree reasonably well with the theory with n_{high} and k_{high} in Eq. 9 at small h, yet the theory overestimates by an increasing amount as h_{th}, or equivalently shear rate, increases. This suggests that the assumption of constant n and k in the extrapolated region ($\dot{\gamma} > 386/\text{s}$) may not be valid, especially at very high shear rates. Furthermore, Eq. 9 indicates $h \sim V^{2n/(1+2n)}$, suggesting that we can deduce n from the $h-V$ relationship. Some representative experiments in Figure 19a were replotted in Figure 19b and their exponents suggest $n \approx 0.17$ for $\phi \leq 0.061$. This value is inconsistent with the assumed $n=n_{\text{high}} \approx 0.4$ and the weak iridescence in our dispersions. Because the fitting assumes V as the only variable in each set of experiments, the deduced n will be inaccurate if n in fact also varies. Both of the above suggest that n is unlikely constant at n_{high} in the extrapolated regime ($\dot{\gamma} > 386/\text{s}$). Instead, we believe that n increases progressively with shear rate as high shear destroys order in deionized colloidal dispersions. Such increasing deviation from n_{high} can likely explain the increasing difference between h_{th} and h_{expt} as shear rate increases (Figure 19a).

We also observed that the films deposited from moderately ordered colloids are quite different at low and high concentrations. As shown in Figure 19b, the film thickness of SiO_2 increases with velocity for lower $\phi(\leq 0.061)$ but is relatively constant for higher $\phi(\geq 0.071)$. We investigated the possible association of the constant thickness with the dynamic yield stress τ_y, which appears as a constant stress at low shear rates.[100] However, we did not find a direct correlation between them. The experimental thickness h_{expt} is in fact about 3–7 times thicker than expected from rheology. Instead, we found that the maximum shear stress deduced from the flow-coating model ($\tau_{\max}=k(\dot{\gamma}_{\max})^n$) exceeded τ_y in all experiments and their ratio $\tau_{\max}/\tau_y$ was smallest for the

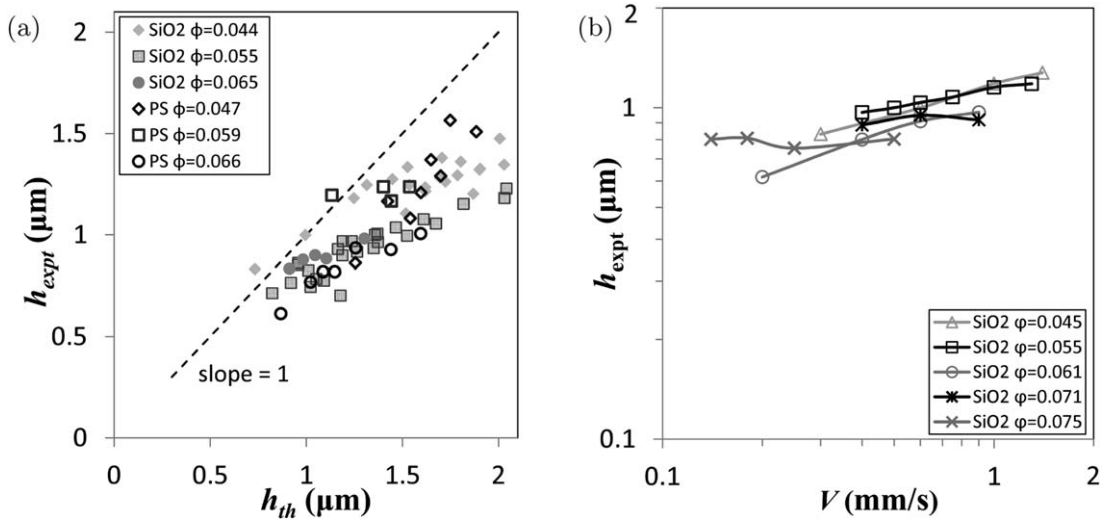

Figure 19. (a) Comparison between experimental (h_{expt}) and theoretical (h_{th}) film thickness from moderately ordered SiO_2 (filled symbols) and PS (open symbols).

h_{th} were calculated using $n=n_{\text{high}}$ and $k=k_{\text{high}}$ in the extrapolated regime. Dashed line indicates $h_{\text{expt}}=h_{\text{th}}$. (b) Film thickness of moderately ordered deionized SiO_2 increases with V at low volume fractions ($\phi \leq 0.061$) and is independent of V at high volume fractions ($\phi \geq 0.071$).

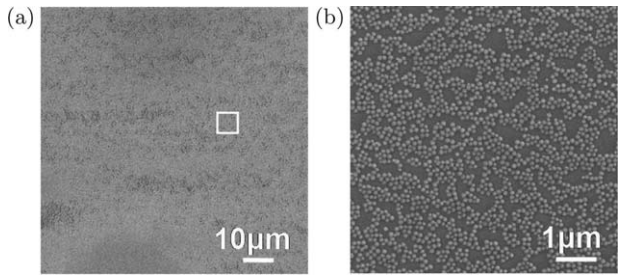

Figure 20. SEM images of sample deposited from moderately ordered SiO_2.

The white box in (a) represents the typical size and location of where (b) and subsequent SEM images are taken.

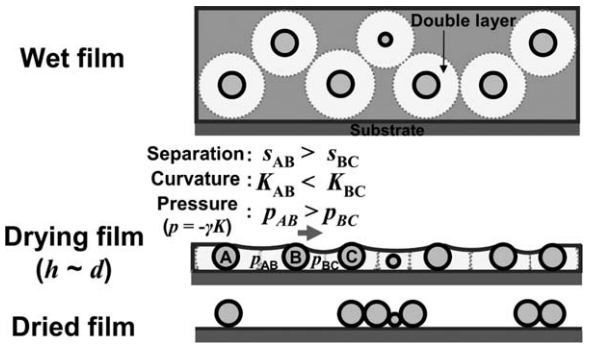

Figure 22. Schematics of ordering during evaporation of deionized moderately ordered colloids deposited at high shear.

high ϕ experiments. This might suggest that the maximum shear stress only determines the film thickness when the ratio τ_{max}/τ_y exceeds a certain threshold. Otherwise, the colloidal dispersion maintains a constant stress which results in the constant film thickness as shown in high ϕ experiments.

Particle Order in Films Deposited from Moderately Ordered Colloids. The SEM images of the deposited particles show that the deionized particles arrange very differently from the nondeionized ones. Comparison between Figure 20 and its counterpart from nondeionized dispersion with similar a (Figure 9b) shows that the latter has larger and more condensed uncovered (dark) area. In spite of the different appearance, the particles do not stack on each other at submonolayer coverage. Therefore, it is still valid to deduce the film thickness h_{expt} from the projected areal coverage a, $h_{expt} = 2ad/(3\phi)$, as mentioned previously.

Besides the different appearance, the quantitative analysis of maximum domain size also shows a different behavior from deionized particles. In particular, while the maximum domain size is inversely correlated with a for nondeionized particles (Figure 13), but increases with a for the deionized particles at all tested volume fractions (Figure 21). Both qualitative and quantitative results suggest the ordering of deionized colloids is not driven only by the lateral capillary pressure.

The weak iridescence and the power law indices $0.4 < n < 1$ deduced from the previous section suggest that the colloids are moderately or poorly ordered in the deposited wet film as depicted in Figure 22. The repulsive double layers cannot generate long-range order in this kinetically trapped configuration. Hence, the interparticle distances are probably nonuniform, resulting in nonuniform curvatures of menisci and capillary pressures as the film dries to $h \sim d$. The lateral capillary pressure gradient pulls the particles together, but the electrostatic repulsion maintains the separation at low to modest coverages (Figure 21, left). As a increases and the particles approach each other, the number of nearest neighbors increases toward the six in ordered domains. This phenomenon is evident when comparing the SEM images at high a (Figure 21, right) with those at low a (Figure 21, left).

Furthermore, the SEM images reveal that the double layers amplify the disadvantage of colloidal polydispersity in packing. Contrary to the size segregation in nondeionized samples (Figure 13, right), the smaller polydispersed particles are intermixed in the deionized system (Figure 21, right). As the film thins to the core diameter of larger particles, the film is no longer thicker than the effective diameter ($d_{eff} = d + 2\kappa^{-1}$) of the smaller particles even though they might have core that is smaller than the film thickness. Therefore, these particles are not free to diffuse to the grain boundaries and are confined within larger particles pulled together by the lateral capillary pressure gradient. The presence of these smaller particles disrupts the packing and leads to smaller domains. The schematics of the ordering are shown in Figure 22.

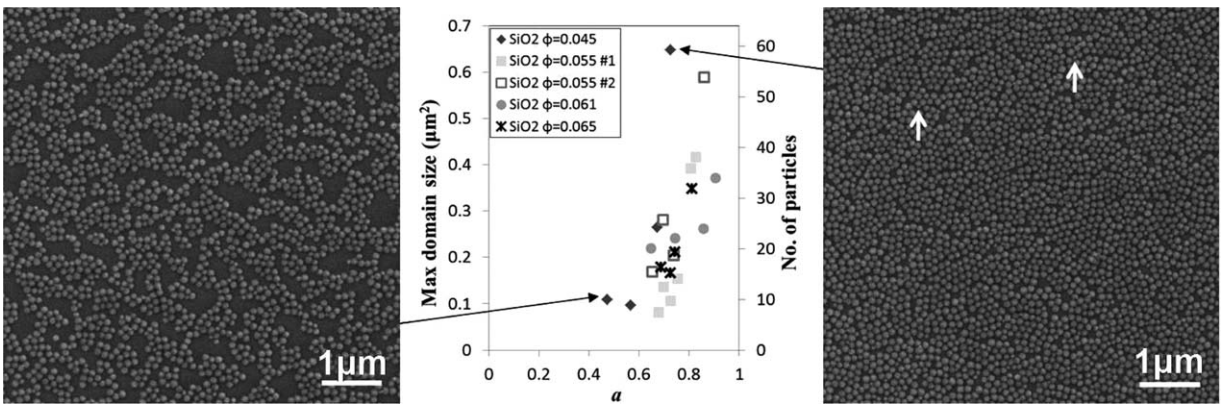

Figure 21. The maximum domain size in a 6.5 μm by 6.5 μm SEM image for deionized SiO_2 that is originally moderately ordered.

The maximum domain size increases with the projected areal coverage a (middle). SEM images of films with low (left) and high (right) overall coverages. Arrows on the right indicate some smaller particles intermixed with the larger monodispersed particles.

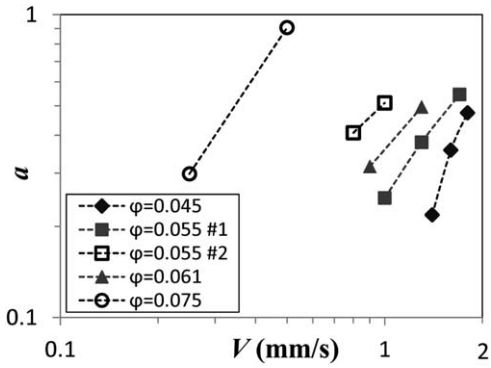

Figure 23. The areal coverage of deionized highly ordered SiO_2 deposited at various velocities.

In spite of the increase with a, the maximum domain size at monolayer coverage is 0.37 μm^2 for moderately ordered SiO_2. This is slightly smaller than the average 0.61 ± 0.11 μm^2 for nondeionized SiO_2, which could be due to the integration of polydispersed particles. The domain sizes of PS monolayers were too small to make any meaningful comparison. In summary, the particle ordering in monolayer did not increase with moderately ordered colloids.

Deposition of highly ordered colloids (colloidal crystals)

Thickness of Films Deposited from Highly Ordered Colloids. We observed only weak iridescence in the PS dispersions, suggesting a lack of high order. This agrees with the rheological measurements with n at the lowest shear rates larger for PS (0.141) than SiO_2 (0.065) and a sudden jump in viscosity, indicating an order-disorder transition, absent in PS. Therefore, only highly ordered SiO_2 colloids with strong iridescence are reported in this section.

Figure 18b shows that the region with highly ordered colloids (filled symbols) always results in thinner films than the region with moderately ordered colloids (open symbols) which are deposited identically. A unique flow property of highly ordered colloids is the existence of dynamic yield stress τ_y. In particular, previous studies show that low shear stresses near τ_y are quite different from the high shear ones due to slippage.[101,102] Therefore, we will first determine whether the shear stress is comparable to τ_y and then see whether that produces a thinner film.

Because the flow-coating model poorly predicts the deposition of highly ordered colloids, we estimate the shear rate at the blade edge as $0.5V/G$, with V the substrate velocity and G the gap height. The n and k deduced from rheological measurements at the lowest shear ($\dot{\gamma}=1-5/\mathrm{s}$), namely, n_{low} and k_{low}, provide an estimate of the shear stress as $\tau_{\mathrm{est}}=k_{\mathrm{low}}(0.5V/G)^{n_{\mathrm{low}}}$. For depositions of highly ordered colloids, we found the shear stresses to be comparable to the yield stresses, with $\tau_{\mathrm{est}}/\tau_y$ larger than unity but not exceeding 1.17. According to Meeker et al.,[101,102] this ratio determines the effect of slippage on fluid flow. The flow-coating model, which assumes a no-slip boundary condition, thus predicts the thicknesses well at high stresses. On the other hand, wall slip becomes significant at stresses only slightly larger than the yield stress. The resultant flow is then a combination of wall slip and bulk flow. Wall slip reduces the effective velocity at the moving substrate and induces an apparent velocity at the stationary blade, which decreases the effective shear rate as $\dot{\gamma}_{\mathrm{eff}}=0.5(V-2V_s)/G$, with V_s the slip velocity. Because our piranha-cleaned silicon substrate and glass slides have smooth surfaces and the experimental stresses for highly ordered colloids are just above the yield stress, deposition likely takes place at a reduced shear due to slippage.[103,104] The film thickness is, therefore, thinner than the high shear experiments, which can also be verified by assuming a slip boundary condition at the moving substrate in the flow-coating model.[105] Furthermore, increasing V diminishes the effect of slipping, hence the larger effective bulk flow results in a thicker film (or equivalently larger a) as shown in Figure 23. Unfortunately, the relationship between V_s and the substrate velocity V is lacking, preventing a quantitative model for the deposited thickness.

Particle Order in Films Deposited from Highly Ordered Colloids. We characterized the order of particles in the deposited film by the maximum single crystalline domain size in a 6.5 μm by 6.5 μm SEM image. Figure 24 shows that the maximum domain size increases with areal coverage a among all tested ϕ. At low a, the isolation of particles with the repulsive double layer can be accommodated, hence resulting in small domain size (Figure 24, left). As the particle concentration (or equivalently a) increases, the number of nearest neighbors and the domain size increases (Figure 24, right).

The positive correlations between maximum domain size and a (Figure 24) and between a and V (Figure 23) suggest

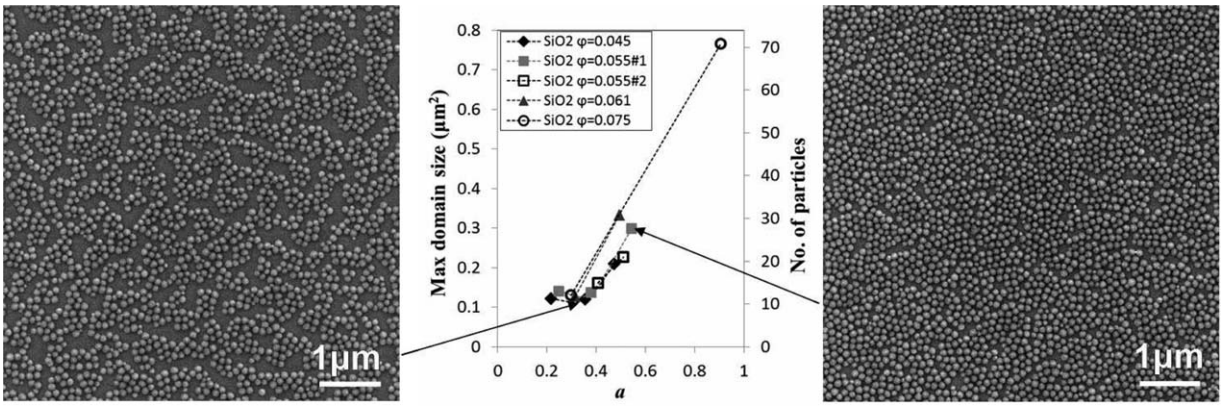

Figure 24. The maximum domain size in a 6.5 μm by 6.5 μm SEM image for deionized SiO_2 that is originally highly ordered.

The maximum domain size increases with projected areal coverage a (middle).SEM images of films with low (left) and high (right) overall coverages.

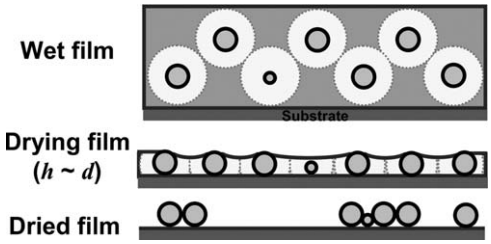

Figure 25. Schematics of ordering during evaporation of colloidal crystal deposited at low shear.

a monolayer of ordered colloids might be achieved with a larger V. However, higher velocities destroy the colloidal crystalline order except at the highest ϕ of 0.075. This is consistent with the linear increase of τ_y with ϕ, suggesting a colloidal crystal from higher ϕ can sustain a larger shear stress before losing the ordered structure. The maximum domain size at monolayer coverage obtained from the highly ordered SiO_2 (0.77 μm^2) exceeds that of moderately ordered particles (0.37 μm^2) but is only slightly larger than for nondeionized particles (0.61 ± 0.11 μm^2). Therefore, the extent of ordered monolayers does not seem to improve with the use of highly ordered deionized particles.

Based on the strong iridescence in the reservoir, we hypothesize the ordered structure of colloidal crystal was minimally disrupted in a low shear deposition (Figure 25). Although the double layers shrink as ion concentration increases about 10-fold during drying as the film dries to $h \sim d$, the double layers are still sufficiently thick to maintain particle order through repulsion. However, as the film dries to $h < d$, capillary pressure dominates and compresses the double layers that generate the order. Hence, the initial particle order was not preserved in the dried film and the final pattern was similar to that from moderately ordered colloids in the previous section. Such a disruption to the original crystalline order immediately prior to complete drying was also observed in evaporative colloid spin-coating.[106] Further studies using *in situ* microscopic and scattering techniques together with high-speed imaging will be useful in confirming the dynamics of particle ordering during film deposition and drying.[106–108]

Colloidal monolayer and the challenges in achieving large domains

Figure 26 compares the SEM images of films with monolayer coverage (a=0.906) obtained from (left to right) high shear deposition of disordered and moderately ordered colloids and low shear deposition of highly ordered colloids. The maximum domain sizes, 0.61 ± 0.11, 0.37 and 0.77 μm^2, respectively, are very similar, indicating that our goal of obtaining large monolayer of ordered particles has not been achieved through Landau–Levich deposition of colloidal crystal from deionization. This reflects the compressibility of the double layer, especially among close-packed particles, and the absence of any long-range guidance to condense individual domains into larger ones as the double layer thickness shrinks. The destruction of order most likely occurs during the final stage of evaporation ($h < d$) when lateral capillary force overshadows the electrostatic repulsive force. Unless the repulsive force that orders the colloids can resist the capillary action, the formation of a large monolayer of ordered colloids by flow-coating remains challenging.

Furthermore, even if we were able to translate the particle order in a wet film to the final dried structure, the inability to predict the film thickness in a low shear deposition of colloidal crystal renders the technique less controllable. In particular, the exact effect of slip velocity on bulk flow and its relationship with substrate velocity is unknown. Without this information, a monolayer can only be achieved through trial and error.

Conclusions

Aqueous silica and polystyrene colloids between 50 and 120 nm were deposited in the Landau–Levich regime using a flow-coating setup. The deposited amount of nondeionized colloids can be controlled well and predicted by the model with a thickening factor that is determined by the Marangoni effect. In particular, large area ($\sim$10 cm^2) of uniform monolayer is achieved. The inverse relationship between the single crystalline domain size of deposited SiO_2 and overall coverage suggests that particle ordering is facilitated by the lateral capillary pressure gradients during film drying. With the depletion of empty space at high coverages, the time allowed for ordering before the film completely dries is reduced. Hence, the domain size at monolayer coverage is not extensive. Furthermore, the domain size of PS is rather small even at low coverages because its hydrophobicity reduces the capillary force that is responsible for nucleating domains. Therefore, a large monolayer of ordered particles, especially hydrophobic ones, cannot be achieved with such a system.

We aimed to improve the particle order through the use of initially ordered colloids, achieved through deionizing the colloidal dispersions and generating long-range repulsions. Rheology characterized the deionized colloidal dispersions

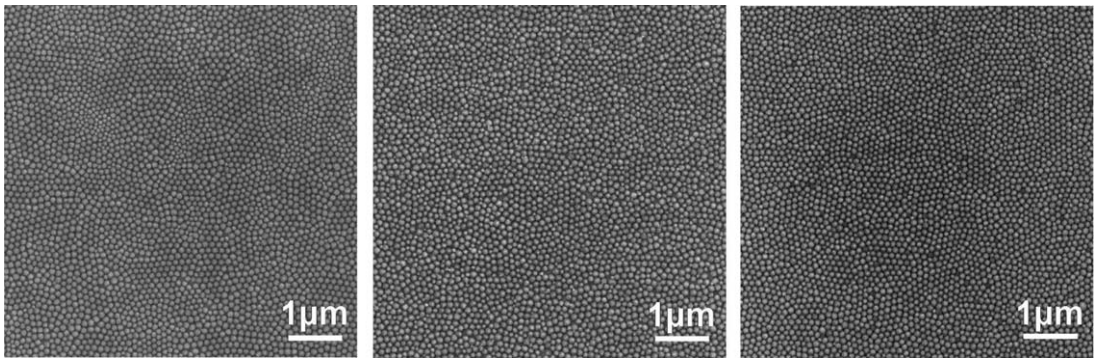

Figure 26. SEM images of SiO_2 monolayer from (left to right) high shear deposition of originally disordered (nondeionized) and moderately ordered colloids, and low shear deposition of originally highly ordered colloids.

as power-law fluids and indicated destruction of order at high shear. We deposited deionized SiO_2 and PS of around 110 nm in both high and low shear regimes. The theoretical thicknesses from the flow-coating model with fixed (extrapolated) power law index n agreed reasonably well with the experimental values but deviated at very high shear, presumably due to progressive destruction of order. The particles were only moderately ordered or poorly ordered in the wet film due to large deformation in the flow field. During a later stage of drying, some particles formed close-packed domains when the lateral capillary attraction overcame the electrostatic repulsion. However, these domains were relatively small because electrostatic repulsion prevented them from merging. At close-packed monolayer coverage, the double layers were highly compressed with no effect on particle order.

On the other hand, we also deposited the colloidal crystal at low shear. Although we were not able to predict the deposited thickness due to the lack of quantified wall slippage, strong iridescence supported that colloidal crystals survived during deposition. However, the ordered structure was not reflected in the final dried film and the domains remained small. We again attributed the poor order to the destruction from nonuniform lateral capillary pressure, which dominated the double layer repulsion during final drying. At this stage, the particles in the film were no longer ordered, like those in the high shear deposition. Hence, their final patterns were similar and the domain size in a close-packed monolayer was not improved.

Acknowledgment

This work was supported by the MRSEC Grant at Princeton University NSF DMR 0819860.

Literature Cited

1. Benisty H, Olivier S, Weisbuch C, Agio M, Kafesaki M, Soukoulis CM, Qiu M, Swillo M, Karlsson A, Jaskorzynska B, Talneau A, Moosburger J, Kamp M, Forchel A, Ferrini R, Houdrá R, Oesterle U. Models and measurements for the transmission of submicron-width waveguide bends defined in two-dimensional photonic crystals. *IEEE J Quantum Electron*. 2002;38:770–785.
2. Chow E, Lin S, Johnson S, Villeneuve P, Joannopoulos J, Wendt JR, Vawter GA, Zubrzycki W, Hou H, Alleman A. Three-dimensional control of light in a two-dimensional photonic crystal slab. *Nature*. 2000;407:983–986.
3. Vukusic P, Sambles JR. Photonic structures in biology. *Nature*. 2003;424:852–855.
4. Barthlott W, Neinhuis C. Purity of the sacred lotus, or escape from contamination in biological surfaces. *Planta*. 1997;202:1–8.
5. Gao X, Yan X, Yao X, Xu L, Zhang K, Zhang J, Yang B, Jiang L. The dry-style antifogging properties of mosquito compound eyes and artificial analogues prepared by soft lithography. *Adv Mater*. 2007;19:2213–2217.
6. Dickey EC, Varghese OK, Ong KG, Gong D, Paulose M, Grimes CA. Room temperature ammonia and humidity sensing using highly ordered nanoporous alumina films. *Sensors*. 2002;2:91–110.
7. Okamoto T, Yamaguchi I, Kobayashi T. Local plasmon sensor with gold colloid monolayers deposited upon glass substrates. *Opt Lett*. 2000;25:372–374.
8. Chou SY, Wei MS, Krauss PR, Fischer PB. Single-domain magnetic pillar array of 35 nm diameter and 65 Gbits/in.^{2} density for ultrahigh density quantum magnetic storage. *J Appl Phys*. 1994;76:6673–6675.
9. Spasova M, Wiedwald U, Ramchal R, Farle M, Hilgendorff M, Giersig M. Magnetic properties of arrays of interacting co nanocrystals. *J Magn Magn Mater*. 2002;240:40–43.
10. Sun S, Anders S, Thomson T, Baglin JEE, Toney MF, Hamann HF, Murray CB, Terris BD. Controlled synthesis and assembly of fept nanoparticles. *J Phys Chem B*. 2003;107:5419–5425.
11. Ee YK, Arif RA, Tansu N, Kumnorkaew P, Gilchrist JF. Enhancement of light extraction efficiency of ingan quantum wells light emitting diodes using SiO_2/polystyrene microlens arrays. *Appl Phys Lett*. 2007;91:221107.
12. Kumnorkaew P, Ee YK, Tansu N, Gilchrist JF. Investigation of the deposition of microsphere monolayers for fabrication of microlens arrays. *Langmuir*. 2008;24:12150–12157.
13. Yang SM, Jang SG, Choi DG, Kim S, Yu HK. Nanomachining by colloidal lithography. *Small*. 2006;2:458–475.
14. Homonnay N, Geyer N, Fuhrmann B, Leipner HS. Advanced colloidal lithography for sub-100 nm lift-off structures. *Vacuum*. 2012;86:1232–1234.
15. Li B, Fang X, Luo H, Seo YS, Petersen E, Ji Y, Rafailovich M, Sokolov J, Gersappe D, Chu B. Separation of DNA with different configurations on flat and nanopatterned surfaces. *Anal Chem*. 2006;78:4743–4751.
16. Chan YC, Lee YK, Zohar Y. Pillar size effect on DNA electrophoresis in microchips with sub-micron pillar arrays. *Proceedings of IEEE International Conference on Micro Electro Mechanical Systems*. Hyogo, Japan, Institute of Electrical and Electronics Engineers (IEEE) Conf. 2007:413–416.
17. Chen K, Azhar E, Ma T, Jiang H, Yu H. Facile large-area photolithography of periodic sub-micron structures using a self-formed polymer mask. *Appl Phys Lett*. 2012;100:233503.
18. Shao DB, Chen SC. Surface-plasmon-assisted nanoscale photolithography by polarized light. *Appl Phys Lett*. 2005;86:253107.
19. Levenson M, Viswanathan NS, Simpson R. Improving resolution in photolithography with a phase-shifting mask. *IEEE Trans Electron Dev*. 1982;29:1828–1836.
20. Tseng A, Chen K, Chen C, Ma K. Electron beam lithography in nanoscale fabrication: recent development. *IEEE Trans Electron Packaging Manuf*. 2003;26:141–149.
21. Su YW, Wu CS, Chen CC, Chen CD. Fabrication of two-dimensional arrays of cdse pillars using e-beam lithography and electrochemical deposition. *Adv Mater*. 2003;15:49–51.
22. Chou SY, Krauss PR, Renstrom PJ. Nanoimprint lithography. *J Vac Sci Technol B*. 1996;14:4129–4133.
23. Byeon KJ, Hwang SY, Lee H. Fabrication of two-dimensional photonic crystal patterns on gan-based light-emitting diodes using thermally curable monomer-based nanoimprint lithography. *Appl Phys Lett*. 2007;91:091106.
24. Velev OD, Gupta S. Materials fabricated by micro- and nanoparticle assembly the challenging path from science to engineering. *Adv Mater*. 2009;21:1897–1905.
25. Brust M, Walker M, Bethell D, Schiffrin DJ, Whyman R. Synthesis of thiol-derivatised gold nanoparticles in a two-phase liquid-liquid system. *J Chem Soc Chem Commun*. 1994;(7):801–802.
26. Martin MN, Basham JI, Chando P, Eah SK. Charged gold nanoparticles in non-polar solvents: 10-min synthesis and 2d self-assembly. *Langmuir*. 2010;26:7410–7417.
27. Bosma G, Pathmamanoharan C, Hoog EH, Kegel WK, Blaaderen A, Lekkerkerker HN. Preparation of monodisperse, fluorescent pmmalatex colloids by dispersion polymerization. *J Colloid Interface Sci*. 2002;245:292–300.
28. Camli ST, Buyukserin F, Balci O, Budak GG. Size controlled synthesis of sub-100nm monodisperse poly(methylmethacrylate) nanoparticles using surfactant-free emulsion polymerization. *J Colloid Interface Sci*. 2010;344:528–532.
29. Matijevic E. Uniform inorganic colloid dispersions. *achievements and challenges. Langmuir*. 1994;10:8–16.
30. Pei W, Kakibe S, Ohta I, Takahashi M. Controlled monodisperse fe nanoparticles synthesized by chemical method. *IEEE Trans Magn*. 2005;41:3391–3393.
31. Xie J, Peng S, Brower N, Pourmand N, Wang SX, Sun S, et al. One-pot synthesis of monodisperse iron oxide nanoparticles for potential biomedical applications. *Pure Appl Chem*. 2006;78:1003–1014.
32. Trau M, Saville DA, Aksay IA. Field-induced layering of colloidal crystals. *Science*. 1996;272:706–709.
33. Dickerson J. *Nanostructure Science and Technology: Electrophoretic Deposition of Nanomaterials*. New York: Springer, 2012.
34. Jiang P, Prasad T, McFarland MJ, Colvin VL. Two-dimensional nonclose-packed colloidal crystals formed by spincoating. *Appl Phys Lett*. 2006;89:011908.
35. Johnston-Peck AC, Wang J, Tracy JB. Formation and grain analysis of spin-cast magnetic nanoparticle monolayers. *Langmuir*. 2011;27:5040–5046.

36. Jung BG, Min SH, Kwon CW, Park SH, Kim KB, Yoon TS. Colloidal nanoparticle-layer formation through dip-coating: effect of solvents and substrate withdrawing speed. *J Electrochem Soc*. 2009;156:K86–K90.
37. Song JH, Harbottle D, Lee JW. Rapid assembly of colloidal monolayer for the synthesis of surface anisotropic particles. *ACS Appl Mater Interfaces*. 2011;3:2392–2397.
38. Brouwer EAM, Kooij ES, Wormeester H, Poelsema B. Ionic strength dependent kinetics of nanocolloidal gold deposition. *Langmuir*. 2003;19:8102–8108.
39. Bandyopadhyay K, Patil V, Vijayamohanan K, Sastry M. Adsorption of silver colloidal particles through covalent linkage to self-assembled monolayers. *Langmuir*. 1997;13:5244–5248.
40. Stafford CM, Roskov KE, Epps TH III, Fasolka MJ. Generating thickness gradients of thin polymer films via flow coating. *Rev Sci Instrum*. 2006;77:023908.
41. Le Berre M, Chen Y, Baigl D. From convective assembly to Landau-Levich deposition of multilayered phospholipid films of controlled thickness. *Langmuir*. 2009;25:2554–2557.
42. Mittal M, Niles RK, Furst EM. Flow-directed assembly of nanostructured thin films from suspensions of anisotropic titania particles. *Nanoscale*. 2010;2:2237–2243.
43. Polsen ES, Bedewy M, Hart AJ. Decoupled control of carbon nanotube forest density and diameter by continuous-feed convective assembly of catalyst particles. *Small*. 2013;9:2564–2575.
44. Kolle M. *Photonic Structures Inspired by Nature*. Heidelberg: Springer, 2011.
45. Born P, Munoz A, Cavelius C, Kraus T. Crystallization mechanisms in convective particle assembly. *Langmuir*. 2012;28:8300–8308.
46. Malaquin L, Kraus T, Schmid H, Delamarche E, Wolf H. Controlled particle placement through convective and capillary assembly. *Langmuir*. 2007;23:11513–11521.
47. Born P, Blum S, Munoz A, Kraus T. Role of the meniscus shape in large-area convective particle assembly. *Langmuir*. 2011;27:8621–8633.
48. Prevo BG, Velev OD. Controlled, rapid deposition of structured coatings from micro- and nanoparticle suspensions. *Langmuir*. 2004;20:2099–2107.
49. Kumnorkaew P, Gilchrist JF. Effect of nanoparticle concentration on the convective deposition of binary suspensions. *Langmuir*. 2009;25:6070–6075.
50. Kleinert J, Kim S, Velev OD. Electric-field-assisted convective assembly of colloidal crystal coatings. *Langmuir*. 2010;26:10380–10385.
51. Prevo BG, Fuller JC, Velev OD. Rapid deposition of gold nanoparticle films with controlled thickness and structure by convective assembly. *Chem Mater*. 2005;17:28–35.
52. Kim MH, Im SH, Park OO. Fabrication and structural analysis of binary colloidal crystals with two-dimensional superlattices. *Adv Mater*. 2005;17:2501–2505.
53. Dimitrov AS, Nagayama K. Continuous convective assembling of fine particles into two-dimensional arrays on solid surfaces. *Langmuir*. 1996;12:1303–1311.
54. Dimitrov AS, Miwa T, Nagayama K. A comparison between the optical properties of amorphous and crystalline monolayers of silica particles. *Langmuir*. 1999;15:5257–5264.
55. Landau L, Levich B. Dragging of a liquid by a moving plate. *Acta Physicochim URSS*. 1942;17:42–54.
56. Brewer DD, Shibuta T, Francis L, Kumar S, Tsapatsis M. Coating process regimes in particulate film production by forced-convection-assisted drag-out. *Langmuir*. 2011;27:11660–11670.
57. Wang Y, Chen L, Yang H, Guo Q, Zhou W, Tao M. Large-area self assembled monolayers of silica microspheres formed by dip coating. *Mater Sci Poland*. 2010;28:467–478.
58. Ghosh M, Fan F, Stebe KJ. Spontaneous pattern formation by dip coating of colloidal suspensions on homogeneous surfaces. *Langmuir*. 2007;23:2180–2183.
59. Brasjen B, Cuijk A, Darhuber A. Dip-coating of chemically patterned surfaces. *Chem Eng Process Process Intensif*. 2011;50:565–568.
60. Fustin CA, Glasser G, Spiess HW, Jonas U. Parameters influencing the templated growth of colloidal crystals on chemically patterned surfaces. *Langmuir*. 2004;20:9114–9123.
61. Oshima H, Tamura H, Takeuchi M, Inomata A, Yanagida Y, Matsushita N, Komoriya H, Uzumaki T, Tanaka A. Nanopattern transfer from high-density self-assembled nanosphere arrays on prepatterned substrates. *Nanotechnology*. 2009;20:455303.
62. Russel W, Saville D, Schowalter W. *Colloidal Dispersions*. Cambridge: Cambridge University Press, 1992.
63. Okubo T. Extraordinary behavior in the structural properties of colloidal macroions in deionized suspension and the importance of the debye screening length. *Acc Chem Res*. 1988;21:281–286.
64. Somasundaran P. *Encyclopedia of Surface and Colloid Science*. Boca Raton: Taylor & Francis Group, 2006.
65. Goldfinger G. *Clean surfaces: Their Preparation and Characterization for Interfacial Studies*. New York: Marcel Dekker, 1970.
66. Pieranski P. Colloidal crystals. *Contemp Phys*. 1983;24:25–73.
67. Goodwin JW, Ottewill RH, Parentich A. Optical examination of structured colloidal dispersions. *J Phys Chem*. 1980;84:1580–1586.
68. Hachisu S, Kobayashi Y, Kose A. Phase separation in monodisperse latexes. *J Colloid Interface Sci*. 1973;42:342–348.
69. Monovoukas Y, Gast AP. The experimental phase diagram of charged colloidal suspensions. *J Colloid Interface Sci*. 1989;128:533–548.
70. Bretherton FP. The motion of long bubbles in tubes. *J Fluid Mech*. 1961;10:166–188.
71. Tallmadge JA, Gutfinger C. Entrainment of liquid films-drainage, withdrawal, and removal. *Ind Eng Chem*. 1967;59:18–34.
72. Wilson S. The drag-out problem in film coating theory. *J Eng Math*. 1982;16:209–221.
73. Maleki M, Reyssat M, Restagno F, Quéré D, Clanet C. Landau-levich menisci. *J Colloid Interface Sci*. 2011;354:359–363.
74. Bullard JW, Garboczi EJ. Capillary rise between planar surfaces. *Phys Rev E*. 2009;79:011604.
75. Hillebrand R, Müller F, Schwirn K, Lee W, Steinhart M. Quantitative analysis of the grain morphology in self-assembled hexagonal lattices. *ACS Nano*. 2008;2:913–920.
76. Forney CF, Brandl DG. Control of humidity in small controlled-environment chmbers using glycerol-water solutions. *HortTechnology*. 1992;2:52–54.
77. Bohren C, Clothiaux E. *Fundamentals of Atmospheric Radiation*. Weinheim: Wiley, 2006.
78. Booth F. The electroviscous effect for suspensions of solid spherical particles. *Proc R Soc London A*. 1950;203:533–551.
79. Russel WB. Low-shear limit of the secondary electroviscous effect. *J Colloid Interface Sci*. 1976;55:590–604.
80. Russel W. *The Dynamics of Colloidal Systems*. Madison: University of Wisconsin Press, 1987.
81. Evans DJ, Hanley HJM, Hess S. Non-newtonian phenomena in simple fluids. *Phys Today*. 1984;37:26–33.
82. Taylor GI. Stability of a viscous liquid contained between two rotating cylinders. *Philos Trans R Soc London A*. 1923;223:289–343.
83. Chen LB, Chow MK, Ackerson BJ, Zukoski CF. Rheological and microstructural transitions in colloidal crystals. *Langmuir*. 1994;10:2817–2829.
84. Imhof A, Blaaderen A, Dhont JKG. Shear melting of colloidal crystals of charged spheres studied with rheology and polarizing microscopy. *Langmuir*. 1994;10:3477–3484.
85. Lindsay HM, Chaikin PM. Shear elasticity and viscosity in colloidal crystals and liquids. *J Phys Colloques*. 1985;46:269–280.
86. Persello J, Magnin A, Chang J, Piau JM, Cabane B. Flow of colloidal aqueous silica dispersions. *J Rheol*. 1994;38:1845–1870.
87. Okubo T. The viscosity of colloidal spheres in deionized suspension the importance of charge density and monodispersity of polystyrene spheres. *Polym Bull*. 1988;20:269–276.
88. Krechetnikov R, Homsy GM. Experimental study of substrate roughness and surfactant effects on the landau-levich law. *Phys Fluids*. 2005;17:102108.
89. Tiwari N, Davis JM. Theoretical analysis of the effect of insoluble surfactant on the dip coating of chemically micropatterned surfaces. *Phys Fluids*. 2006;18:022102.
90. Ramdane OO, Quéré D. Thickening factor in marangoni coating. *Langmuir*. 1997;13:2911–2916.
91. Shen AQ, Gleason B, McKinley GH, Stone HA. Fiber coating with surfactant solutions. *Phys Fluids*. 2002;14:4055–4068.
92. Park CW. Effects of insoluble surfactants on dip coating. *J Colloid Interface Sci*. 1991;146:382–394.
93. Berg J, Acrivos A. The effect of surface active agents on convection cells induced by surface tension. *Chem Eng Sci*. 1965;20:737–745.
94. Deegan RD, Bakajin O, Dupont TF, Huber G, Nagel SR, Witten TA. Contact line deposits in an evaporating drop. *Phys Rev E*. 2000;62:756–765.

95. Kralchevsky P, Paunov V, Ivanov I, Nagayama K. Capillary meniscus interaction between colloidal particles attached to a liquidfluid interface. *J Colloid Interface Sci*. 1992;151:79–94.
96. Denkov N, Velev O, Kralchevski P, Ivanov I, Yoshimura H, Nagayama K. Mechanism of formation of two-dimensional crystals from latex particles on substrates. *Langmuir*. 1992;8:3183–3190.
97. Dimitrov AS, Dushkin CD, Yoshimura H, Nagayama K. Observations of latex particle two-dimensional-crystal nucleation in wetting films on mercury, glass, and mica. *Langmuir*. 1994;10:432–440.
98. Pontoni D, Alvine KJ, Checco A, Gang O, Ocko BM, Pershan PS. Equilibrating nanoparticle monolayers using wetting films. *Phys Rev Lett*. 2009;102:016101.
99. Kralchevsky PA, Nagayama K. Capillary forces between colloidal particles. *Langmuir*. 1994;10:23–36.
100. Mewis J, Wagner N. *Colloidal Suspension Rheology*. New York: Cambridge University Press, 2011.
101. Meeker SP, Bonnecaze RT, Cloitre M. Slip and flow in soft particle pastes. *Phys Rev Lett*. 2004;92:198302.
102. Meeker SP, Bonnecaze RT, Cloitre M. Slip and flow in pastes of soft particles: direct observation and rheology. *J Rheol*. 2004;48:1295–1320.
103. Tabuteau H, Baudez JC, Bertrand F, Coussot P. Mechanical characteristics and origin of wall slip in pasty biosolids. *Rheol Acta*. 2004;43:168–174.
104. Ballesta P, Petekidis G, Isa L, Poon WCK, Besseling R. Wall slip and flow of concentrated hard-sphere colloidal suspensions. *J Rheol*. 2012;56:1005–1037.
105. Dutta A, Mashelkar R. On slip effect in free coating of non-newtonian fluids. *Rheol Acta*. 1982;21:52–61.
106. Giuliani M, Gonzlez-Vias W, Poduska KM, Yethiraj A. Dynamics of crystal structure formation in spin-coated colloidal films. *J Phys Chem Lett*. 2010;1:1481–1486.
107. Ebbens S, Hodgkinson R, Parnell AJ, Dunbar A, Martin SJ, Topham PD, Clarke N, Howse JR. In situ imaging and height reconstruction of phase separation processes in polymer blends during spin coating. *ACS Nano*. 2011;5:5124–5131.
108. Toolan DTW, Parnell AJ, Topham PD, Howse JR. Directed phase separation of PFO:PS blends during spin-coating using feedback controlled in situ stroboscopic fluorescence microscopy. *J Mater Chem A*. 2013;1:3587–3592.

Manuscript received Sept. 16, 2013, and revision received Jan. 21, 2014.